An integrated geomechanical and petrophysical multiparameter approach for gas reservoir evaluation

Or Aimon Brou Koffi Kablan[1] · Tongjun Chen[1]

Abstract

Integrating petrophysical and geomechanical parameters is an efficient approach to evaluating shale gas reservoir potential. The high cost of corings and their limited number, coupled with time-intensive investigation, led researchers to use this alternative combination approach. In the Jiaoshiba area, from single-pilot well core data and log measurements, petrophysical and geomechanical parameters such as shale volume, total organic carbon, gas content, as well as pore pressure, stress components, and mineral brittleness were first estimated using established methods. In the second phase, based on logging curves, the reservoir electro-facies (EF) classification was performed using the unsupervised multi-resolution graph-based clustering method on a series of twenty wells, identifying five EF with different intrinsic characteristics. Unsupervised analyses were developed using the multilayer artificial neural network while incorporating the K-nearest neighbors and graphical classification algorithms. The results from the first and second phases indicate reservoir richness in organic matter, with the best reservoir exhibited by EF2 and EF3. In addition, effective stress components (S_V, S_H, and S_h) evaluation shows a normal stress regime with hydraulic fracture systems perpendicular to the minimum horizontal stress at each measured depth of the reservoir ($S_v > S_H > S_h$). This research workflow can efficiently evaluate shale reservoirs with a realistic approach for identifying favorable fracturing positions while reducing errors due to human interference.

List of symbols

Latin letters

a_i	Multinominal coefficient at a given temperature
BI	Brittleness index (%)
Dist (x, y)	Euclidian distance between two samples x and y
E	Young's modulus
EE	Eaton exponent (range between 1 and 1.9 for old basins)
G_{ads}	Adsorbed gas (m³/ton)
G_{free}	Free gas in pores (m³/ton)
GR_{index}	Linear gamma ray (GAPI)
G_{total}	Total gas content (m³/ton)
KRI	Kernel representative index
LOM	Indicator of organic matter maturity
NI	Neighboring index function
P_{LT}	Initial volume of absorbed gas (m³)
P_p	Pore pressure (MPa)
pr_i	Reduced pression coefficient
R_c	Gas constant
$s(x)$	Sum of the weighted ranks for a given measurement at point x
S_H	Horizontal maximum stress (MPa)
S_h	Horizontal minimum stress (MPa)
S_v	Vertical stress (MPa)
S_w	Water saturation (%)
T	Reservoir temperature (K)
TOC	Total organic carbon (%)
V	Pore volume (m³/g)
V_{LC}	Gas absorbed in the solid adsorbent (m³)
V_p	Compressional velocity (m/s)
V_s	Shear velocity (m/s)

✉ Tongjun Chen
tjchen@cumt.edu.cn

Or Aimon Brou Koffi Kablan
orkablan@cumt.edu.cn

1 School of Resources and Geosciences, China University of Mining and Technology, Xuzhou 221116, Jiangsu, China

V_{sh}	Shale volume (V/V)
Z	Compressibility factor of methane

Greek letters

α	Biot alpha coefficient (range between 0.3 and 0.8)
ε	Strain factor
ϕ_{eff}	Effective porosity (%)
β	Geomechanical constant ($\beta = 106$)
Δ	Difference between two parameters
μ	Poisson's ratio
ρ	Density (g/cm^3)
υ	Coefficient relative to Poisson's ratio

Abbreviations

AC	Acoustic log
ANN	Artificial neural network
CAL	Caliper log
CNL	Neutron porosity log
DEN	Density log
DT	Sonic log
ECS	Elemental capture spectroscopy
GR	Gamma-ray log
KNN	The K-nearest neighbor
LLD	Deep resistivity log
LLS	Shallow resistivity log
MRGC	Mult-resolution graph-based clustering
NMR	Nuclear magnetic resonance
SOM	Self-organizing map
SP	Spontaneous potential log

Introduction

In recent years, shale gas development activities have expanded from North America to the rest of the world, mainly because of the continued increase in social demand for clean energy, a better understanding of unconventional gas resource accumulation conditions, the rising price of natural gas, and the continuous advancement of drilling technology (Ou et al. 2018; Gou et al. 2021). Shale gas has emerged as an important unconventional natural resource and represents a new bright spot for the oil and gas industries. According to the composition and distribution of China's global resources, the estimated reserves of shale gas are equivalent to conventional gas resources. Moreover, multiple exploration projects were conducted, especially in the Sichuan Basin from the north to the south, resulting in two phases of gas production in this area (Chen et al. 2018). However, systematic techniques are required to increase the efficacy of exploration and production in order to satisfy the continued demands of the market (Sakhaee-Pour and Bryant 2012; Hu et al. 2018). Consequently, different workflows for integrating petrophysical and geomechanical

parameters are essential for an accurate reservoir evaluation. The development of a model that combines the petrophysical and geomechanical characteristics of shale rock has a significant impact on engineering applications, such as gas reserve evaluation, rock properties determination, and field development (Alipour et al. 2021; Song et al. 2023).

Many research works combining petrophysical and geomechanical data on distinct segments of China recoverable shale gas resources were conducted using different methods to characterize reservoirs (Dong et al. 2018; Zheng et al. 2018; Jia et al. 2021; Nie et al. 2021; Xiong et al. 2022). These studies indicated that petrophysical characteristics, essentially shale volume (V_{sh}), porosity (CNL), total organic carbon (*TOC*), and gas content (G_{total}), can be obtained from standard procedures. V_{sh} is often calculated using the linear gamma-ray shale volume expression, while porosity is commonly estimated using basic logging data such as formation resistivity (LLD), sonic (DT), acoustic (AC), density (DEN), and nuclear magnetic resonance (NMR) or by cross-plots of DT, DEN, and CNL logs. *TOC*, which corresponds to the organic richness of the rock, is determined using core testing, wireline logging curves, or by combining the two methods (Liu et al. 2020). Zhu et al. (2018) used the Passey et al. (1990) method, coupled with results from X-ray diffraction (XRD) core analysis and mineral models, to estimate organic-rich source rock. G_{total} was typically obtained from core data analysis through the element capture spectrum (ECS) coupled with the formation micro-imager tests (FMI), as the presence of gas in shales is in the form of free phase within pores and fractures and as gas sorbed onto organic matter (Yu et al. 2018; Alipour et al. 2022).

Geomechanical characterization includes pore pressure (P_p), brittleness index (*BI*), and in situ stress (S_v, S_H, and S_h), which are critical indicators for shale gas reservoir hydraulic fracturing. Different concepts and empirical equations were used to evaluate these parameters (Meng et al. 2020; Qian et al. 2020; Xia et al. 2022). *BI* was determined using a measure of rock energy consumption during drilling processes (mechanical approach) or by physical measurements of rock properties (mineralogical composition). The presence of carbonate, feldspar, and quartz is the principal brittleness factor of the reservoir rock; typically, the presence of carbonate and quartz makes the rock more brittle (Mews et al. 2019). The other way to estimate *BI* is in terms of mechanical characteristics, which suggests that shale with a lower Poisson's ratio (μ) associated with a high Young's modulus (*E*) tends to be more brittle, highly susceptible to complex fractures, and easy to break. *P*p prediction approaches include the basic Eaton method (Eaton 1975), which derives pore pressure from compressional velocity and acoustic transit time. This approach assumes that porosity decreases as a function of depth in most shale

gas reservoirs, following a trend depending on the normal hydrostatic pressure, fluid pressure, and burial depth, supported by the Terzaghi effective stress principle (Terzaghi et al. 1996). On the other hand, the Bowers approach (Bowers 1995) evaluates reservoir effective stress using overburden pressure data. Previous modeling of S_v, S_H, and S_h in the Sichuan Basin reveals that most in situ stress works were based on well-log interpretations and laboratory measurements (Sakhaee-Pour and Li 2016). The main widely used approaches include the finite element and stress polygon models, which consider the influence of the geo-structure and basin history (Dong et al. 2018; Alipour and Sakhaee-Pour 2023).

These methods, essentially based on relationships between different response parameters (well logs and laboratory measurements), are, in most cases, efficient for a specific segment and under certain assumptions. Jiaoshiba shale gas field is characterized as a complex system (formations and tectonic evolution) with challenges to accurately evaluate the main reservoir properties (Hu et al. 2018; Gou and Xu 2019; Esatyana et al. 2020). Furthermore, these parameters vary horizontally and vertically, making determining their intrinsic characteristics difficult. Therefore, a systematic multiparameter integration approach is necessary to increase the comprehensiveness of reservoir quality.

The present study aimed to propose a model combining petrophysical and geomechanical parameters for a series of wells to find the best reservoir quality in the Jiaoshiba shale gas field. Firstly, the main petrophysical and geomechanical characteristics, including V_{sh}, TOC, G_{total}, Pp, S_v, S_H, S_h, and BI, were estimated based on conventional wireline logging and core testing results for the pilot well. Secondly, classify reservoir EF sequences using the unsupervised multiresolution graph-based clustering (MRGC) method on the set of wells. The unsupervised MRGC method integrates the artificial neural network (ANN), K-nearest neighbors (KNN), and graphical classification algorithms. The results were then correlated and integrated to define and classify the reservoir. The proposed approach can be applied to reduce some time-intensive conventional processes and is efficient for prospect modeling and rock properties characterization.

Geological setting

The Jiaoshiba onshore gas field is on the southeastern margin of the Sichuan Basin, in Southwest China. The geology of this zone is dominated by multiple tectonic movements that cause formations to uplift, accompanied by wide and steep anticline belts along the northeast direction. This stratum underlies the Hanjiadian and Xiaoheba formations and overlies the Jiaocaogou and Baota Ordovician formations (Fig. 1a).

During the late Ordovician period, the continental shelf environment changed from a deep shelf to a shallow shelf in the northeast of the Yangtze area, resulting in the depositional formation of organic-rich shale with abundant graptolites along the northeast direction (Gou et al. 2021; Nie et al. 2021). The Jiaoshiba area environment evolution is characterized by a series of northeast-oriented structural deformations surmounted by faults and fractures associated with two global transgressions developed in the middle part. The Wufeng-Longmaxi formations general mineralogy composition is essentially dominated by siliceous and black carbonaceous, with a lower proportion of carbonate and clay minerals resulting from a series of complex collisions, assemblages, and formations of the Yangtze blocks (Chen et al. 2018).

In the regional stratigraphy, the layers include mudstones, siltstones, and limestones (Fig. 1b), forming a rich organic shale layer that can be classified as a sand-shale system (sand with thinly bedded shales) of deep marine shelf deposits (Hu et al. 2018; Xiong et al. 2022). Figure 1 presents the location and the geological description of the pilot well, named JY-1X, vertically drilled in the Jiaoshiba gas field. This well has a total depth of 2440 m and crosses the Wufeng-Longmaxi formations.

Materials and methods

Data description and workflow

The data from the pilot well JY-1X are composed of conventional wireline logs and core testing results of the Wufeng-Longmaxi for a measured depth range of 2262.3–2372 m, and data from this well were used to calibrate the results. Core sample interpretations were used to describe the shale formation of Wufeng-Longmaxi units. Figure 2 shows an image of core samples from each geological sublayer (reservoir zones) of the pilot well JY-1X before testing. Core test results for the target zone include mineral composition and formation pressure tests. Geological data consist of lithology interpretation and stratification. A total of nine zones, numbered 1#–9#, were identified based on core analysis and logging characteristics. These zones are located between depths ranging from 2262.3 to 2372 m, and their thickness varies between 1.0 and 21.5 m. Samples numbered from S-01 to S-09 correspond to zones 9# to 1# following the sample depth (Table 1). In this study, a total of 20 wells with the necessary well-logs were used for the electro-facies (EF) study. Given the large extension of the research area and the practical impossibility of evaluating core data from all these drilled wells in the Jiaoshiba area, the present study widely used well-log data for this study. Conventional logs, essentially porosity (DEN and CNL), resistivity (LLS and
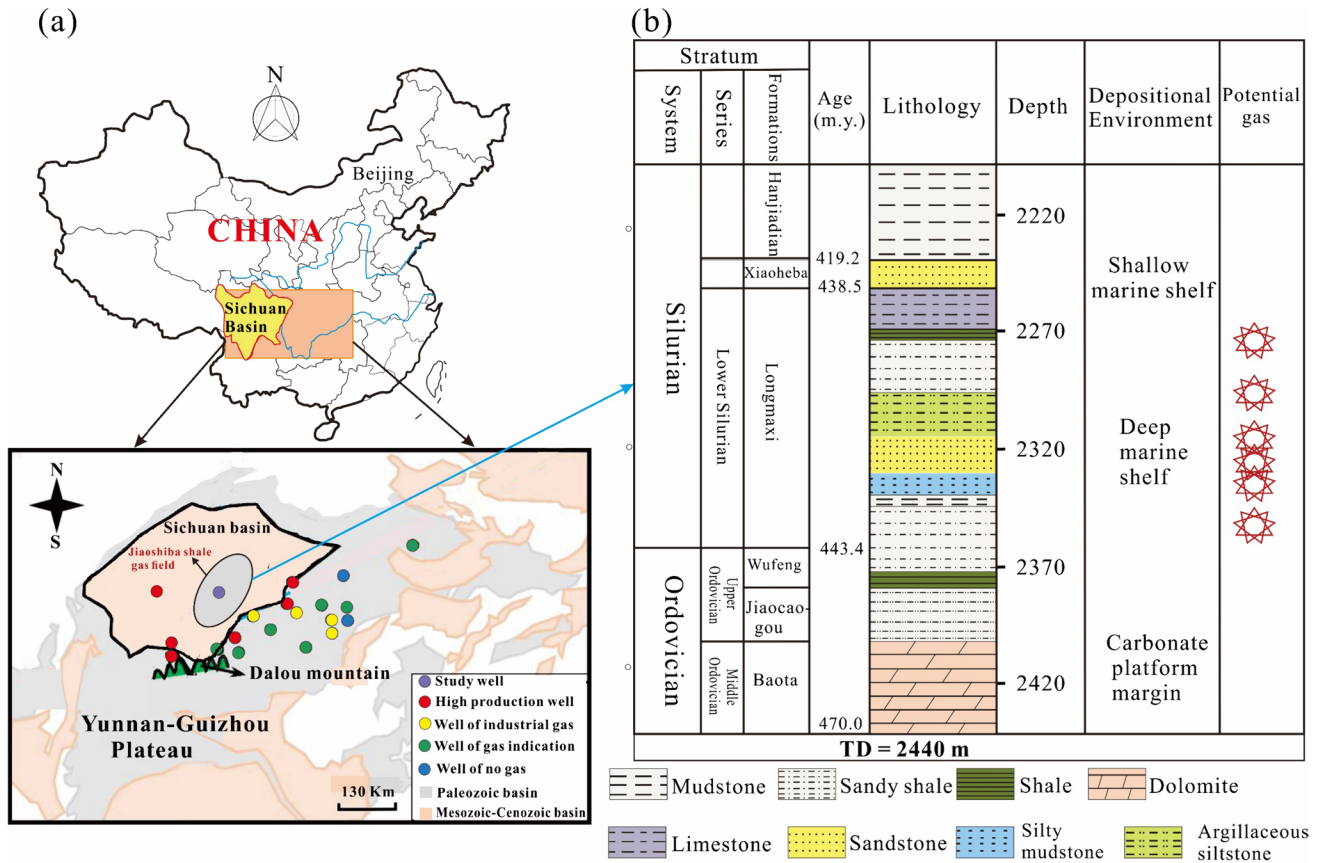
Fig. 1 **a** Location of the Jiaoshiba shale gas field and **b** Description of the reservoir regional stratigraphy and depositional environment. Modified from Gou et al. (2021)

LLD), gamma ray (GR), sonic (DT), spontaneous potential (SP), and acoustic (AC) logs, were available in most of the wells with data that can be considered consistent for this study. Compressional velocity (V_p) and shear wave velocity (V_s) were generated from the inverse of interval travel times from sonic and dipole shear logs, respectively. They were then correlated with DT, CNL, and GR logs to ensure consistency.

Total organic carbon (*TOC*) was evaluated using LLS, LLD, and AC. Horizontal minimum stress (S_h), horizontal maximum stress (S_H), and vertical stress (S_v) were predicted at each depth section after estimating elastic properties from log data. DT was used as an indicator of porosity by recording the interval transit time for the compressional acoustic wave traveling through the formation. The brittleness index (*BI*) was determined by considering CNL, DEN, Vsh, and DEN logging curves to generate Poisson's ratio (μ) and Young's modulus (*E*). The Eaton–Yale pore pressure (P_p) method and formation properties were added to account for the Jiaoshiba thin shaly-sand effect on reservoir complexity. The multi-resolution graph-based clustering method (MRGC) was used to perform multiparameter analysis, predict EF, and comprehensively

evaluate the formation anisotropy of the reservoir. The workflow was implemented in Geolog software, and a summary of these parameters and steps is presented in Fig. 3.

Petrophysical parameters

The most direct and reliable method to determine *TOC* is to use core data for laboratory measurement. However, due to the high cost of coring and the incapacity to obtain continuous data for all wells, conventional log curves to calculate *TOC* appear to be a convenient and accessible method. In this study, *TOC* was calculated using the baseline superposition of LLD and AC difference of the $\Delta \log R$ method (Zhao et al. 2017). Details of this approach are given in Eqs. (1), (2), and (3).

$$\Delta \log R = \log \frac{R}{R_{Base}} + K * \left(\Delta t - \Delta t_{Base} \right) \tag{1}$$

$$K = \frac{\log \left(R_{max} / R_{min} \right)}{\Delta t_{max} - \Delta t_{min}} \tag{2}$$

Fig. 2 Core samples from well JY-1X before geomechanical tests. On the gamma-ray log curve (*left*), sample depths are highlighted with green triangles. The representative cores numbered from S-01 to S-09 (*right*) correspond to sublayers 9# to 1# according to sample depths

Table 1 Reservoir zonation and depth shifts of well JY-1X

Gas layer number	Zone section (m)	Thickness (m)	Formation	Sample	Sample depth (m)
9#	2262.3–2283.8	21.5	Upper Longmaxi	S-01	2278.58
8#	2283.8–2301.3	17.5	Lower Longmaxi	S-02	2290.37
7#	2301.3–2313.3	12.0		S-03	2303.21
6#	2313.3–2322.7	9.4		S-04	2315.94
5#	2322.7–2332.8	10.1		S-05	2325.36
4#	2332.8–2343	10.2		S-06	2339.67
3#	2343–2356.3	13.3		S-07	2349.71
2#	2356.3–2357.3	1.0	Wufeng formation	S-08	2356.60
1#	2357.3–2372	14.7		S-09	2364.25

$$\text{TOC} = (\Delta \log R) * 10^{2.297 - 0.1688 * \text{LOM}} \tag{3}$$

where R is the value of LLD, and $\Delta \log R$ is the differentiation amplitude of LLD and AC curves, which includes source rock characteristics and rock properties. *LOM* is an indicator of organic matter maturity, ranging between 6.0 and 10.5. K is Passey's organic carbon determination coefficient. Δt is the variation in acoustic time measurement. Δt_{Base} and R_{Base} are LLD and AC differences in base values.

Knowing that the linear V_{sh} method tends to overestimate the content of shale in the reservoir (Mkinga et al.

2020), V_{sh} was estimated by computing Clavier equation (Clavier et al. 1971) using GR curve, as described in Eq. (4).

$$V_{\text{sh}} = 1.7 - \sqrt{3.38 - \left(GR_{\text{index}} + 0.7\right)^2} \tag{4}$$

where $GR_{\text{index}} = \frac{GR_{\text{log}} - GR_{\text{ma}}}{GR_{\text{sh}} - GR_{\text{ma}}}$ is the linear V_{sh} from gamma ray, GR_{log} is gamma-ray reading in every depth of the reservoir, GR_{sh} is gamma-ray reading in 100% shale zone, GR_{ma} is gamma-ray response in the 100% matrix rock, and V_{sh} is shale volume (Clavier et al. 1971; Mkinga et al. 2020).

Fig. 3 Workflow used for the study
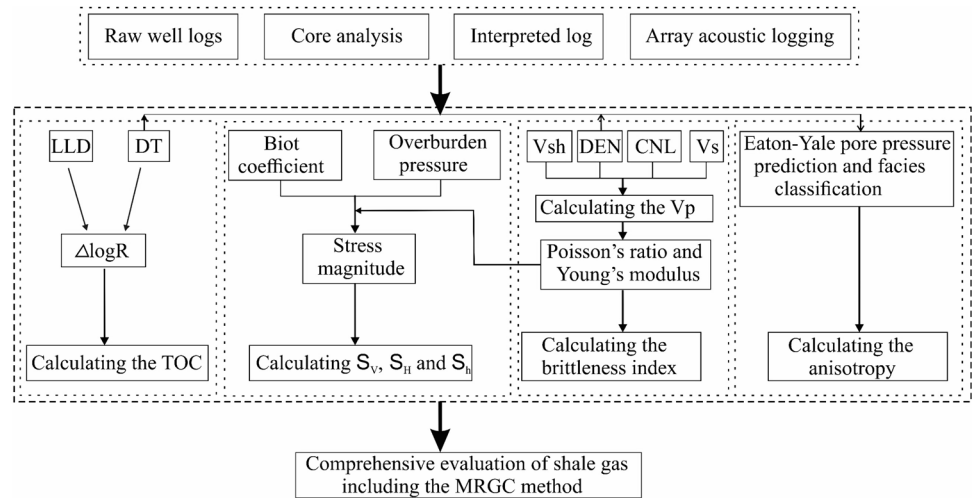
Shale gas is naturally trapped within the pores of this sedimentary rock, as shale is a fine-grained formation that acts as both creator of the gas through the decomposition of organic matter (source) and storage material (reservoir). Gas content was estimated for the pilot well by combining logging and core data, knowing that gas is present and stored in pore spaces and cracks in free and adsorbed states (Shen et al. 2023) (Eq. 5).

$$G_{\text{total}} = G_{\text{free}} + G_{\text{ads}} \tag{5}$$

where G_{total} is total gas content (m³/ton). G_{free} and G_{ads} are free and adsorbed gases, respectively, in pores. The Langmuir isotherm equation was used to determine the volume of adsorbed gas (Eq. 6), assuming that gas attaches to the shale surface, forming a single layer (Gou and Xu 2019; Shen et al. 2023).

$$G_{\text{ads}} = \frac{V_{\text{LC}} \cdot P}{P + P_{\text{LT}}} \tag{6}$$

where P is reservoir pressure, V_{LC} is gas absorbed in the solid adsorbent, and P_{LT} is the initial volume of absorbed gas. G_{free} is computed using the equation related to effective porosity and effective gas saturation (Eqs. 7 and 8), at standard temperature and pressure (60 °F and 14.7 psi).

$$G_{\text{free}} = \frac{\Phi_{\text{eff}} \cdot V \cdot (1 - S_w)}{Z R_c T} \tag{7}$$

$$Z = \sum_{i=0}^{n} a_i pr_i \tag{8}$$

where Z is the compressibility factor of methane, related to pressure and temperature. a_i is the different multinominal coefficients at a given temperature. pr_i is the reduced pressure. ϕ_{eff} is effective porosity, Sw is water saturation, Rc

is gas constant, T is reservoir temperature, and V is pore volume, respectively.

Geomechanical parameters

Mineral brittleness estimation is an essential characteristic in reservoir fracturing operations and can be obtained by different methods. In this study, two different approaches were used to define the rock *BI*. The first approach calculates *BI* using the core data results of brittle mineral fractions such as limestone, dolomite, and quartz in the total amount of shale. The presence of these particular minerals causes shales to become more brittle, and it is easier to develop fracture networks during fracturing operations (Meng et al. 2020; Xia et al. 2022). In contrast, more clay causes shales to become more ductile. Rock mineral composition was provided by the elements capture spectrum (ECS) test combined with the nuclear magnetic resonance (NMR) analysis of the whole rock. In this case, *BI* is quartz and carbonate content ratio to the sum of other minerals (Eq. 9).

$$BI_1 = \frac{w(\text{qz}) + w(\text{car})}{w(\text{qz}) + w(\text{felds}) + w(\text{clay}) + w(\text{car})} \tag{9}$$

where BI_1 is brittleness index obtained from rock mineral composition. *w(qz)* is the content of quartz, w(car) is the content of carbonate minerals, *w(felds)* is the content of feldspar, and *w(clays)* is the content of clay minerals. The second *BI* approach used rock mechanical properties from logging curves (Qian et al. 2020). The calculation method is the Poisson–Young method, which defines *BI* based on μ and *E*. Shale is more brittle with high *E* and low μ (Mews et al. 2019; Liu et al. 2023). The calculation process is described by Eqs. 10–12.

$$\mu = \frac{1}{2} * \frac{\Delta t_s^2 - 2\Delta t_p^2}{\Delta t_s^2 - \Delta t_p^2} \tag{10}$$

$$E = \frac{\rho_b}{\Delta t_s} * \frac{\Delta t_s - \Delta t_p}{\Delta t_s - \Delta t_p} * \beta \tag{11}$$

$$BI_2 = \frac{\left[\frac{100\left(E - E_{min}\right)}{\left(E_{max} - E_{min}\right)} + \frac{100\left(\mu - \mu_{max}\right)}{\left(\mu_{min} - \mu_{max}\right)} \right]}{2} \tag{12}$$

where ρ_b is bulk density, Δt_p is compressional wave time difference (μs/m), Δt_s is the shear wave time difference (μs/m), and β is a mechanical constant equal to 106. The subscripts *min* and *max* refer to the minimum and maximum values of the considered parameters, respectively. This second approach was applied to the other set of wells for the EFs classification. The degree of brittleness was evaluated according to Perez and Kurt (2013) and Omer et al. (2018) classification method. The formations are brittle when *BI* is greater than 48%. Conversely, they are considered less brittle when comprising between 32 and 48%, less ductile when varying from 16 to 32%, and ductile between 0 and 16%.

Pore pressure is a crucial part of shale gas reservoir characterization especially for complex systems due to compaction mechanisms, formation–tectonic evolution, and lithology variations. As the Jiaoshiba area is part of the Sichuan Basin, which is identified as a complex and old basin, the Eaton–Yale pore pressure method (Yale et al. 2018) was used to reliably estimate pore pressure using logging curves. This method extends the Eaton and Bowers methods to more lithified and complex basins while correcting overpressure zones (Eq. 13).

$$P_P = \frac{\left[OBP - \left(OBP - \alpha P_{hyd} \right) * C * \left(\frac{V_i}{V_p} \right)^{EE} \right]}{\alpha} \tag{13}$$

where *Pp* is Eaton–Yale pore pressure, V_i is the porosity corrected by the measured V_p, *OBP* is the overburden pressure, V_p is the lithology adjusted by the V_p normal pressure trendline, and *C* is a calibration factor of the basin. α is Biot alpha coefficient, which varies between 0.3 and 0.8, P_{hyd} is the hydrostatic pressure, and *EE* is Eaton exponent.

The in situ stress profile, which includes S_v, S_H, and S_h, was investigated using different approaches. The magnitude of S_v was computed by integrating rock density from the surface to the bottom of the measured depth profile (Eq. 14).

$$S_V = \int_0^z \rho(z)gdz \approx \rho gz \tag{14}$$

where $\rho(z)$ is depth-dependent density, ρ is average overburden density, and g is the gravitational acceleration constant.

S_H and S_h were computed using the poroelastic theory. The poroelastic theory is effective in reservoir elastic matrix, where variations in reservoir are caused by stress deformation (Gou et al. 2021). The Jiaoshiba area results from tectonic plate movement, which causes tectonic strain and stress within the reservoir, resulting in increased strain and stress components in the rock (Nie et al. 2021). Therefore, S_H and S_h were generated from the relationship between Biot's parameter, overburden stress, pore pressure, and Poisson's ratio (Zoback et al. 2003) (Eqs. 15 and 16).

$$S_h = \frac{\upsilon}{1 - \upsilon}\left(S_v - \alpha P_p\right) + \alpha P_p + \frac{E\varepsilon}{1 - \upsilon^2} \tag{15}$$

$$S_H = \frac{\upsilon}{1 - \upsilon}\left(S_v - \alpha P_p\right) + \alpha P_p + \frac{E\varepsilon}{1 - \upsilon^2} \tag{16}$$

where ε is the strain factor, α is Biot's coefficient (was set to 1), and υ is a coefficient relative to Poisson's ratio. *E* is Young's modulus, and P_p is pore pressure from the Eaton–Yale method.

Clustering implementation

EF classification is an essential component in the identification and characterization of shale reservoirs. Its application contributes to prospect modeling and permits the bypass of some time-consuming stages of unconventional reservoir characterization techniques (Al Hasan et al. 2023). The clustering algorithm recognizes different groups (clusters) of identical properties in a large set of data and attempts to increase the similarity within each cluster while reducing it between different clusters. However, conventional clustering algorithms suffer from essentially three limitations. Firstly, they are very sensitive to the quality and quantity of initial data. Secondly, they give approximative results when the data are not homogeneous or contain inconsistent values. Third, the number of clusters to be differentiated must be known before the start of the computation process (Dos Passos et al. 2020). MRGC was proven to be free of these limitations and better than the conventional clustering method. As a modern clustering method, MRGC is an unsupervised, nonparametric approach that uses an artificial neural network (ANN). The unsupervised algorithm incorporates the K-nearest neighbors (KNN) and graphical classification techniques following a precise computation order process. Typically, the MRGC facies classification and modeling use data distribution density and search space dimensions to identify the number of EF.

In this study, petrophysical parameters (GR and *TOC*) and geomechanical characteristics (BI_2, S_v, S_H, and S_h) were selected for the set of wells to classify the reservoir using MRGC. These parameters account for key reservoir

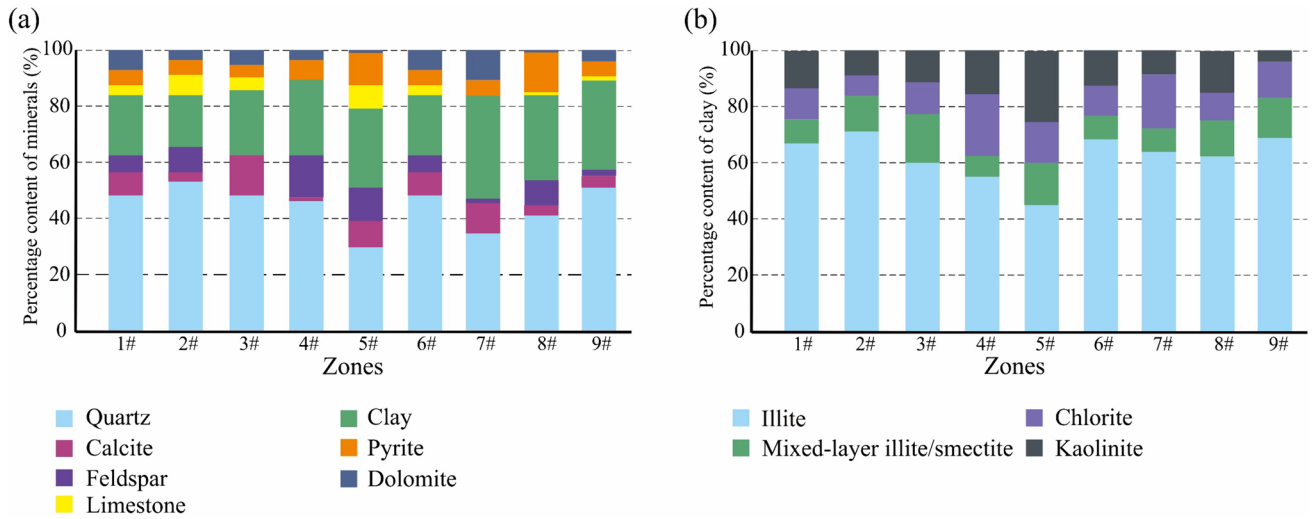**Fig. 4** Histograms showing **a** mineral content and **b** clay mineral composition in well JY-1X

Table 2 Results of the quantitative minerals analysis

Layer number	Zone section meter (m)	Siliceous (%)	Clay (%)	Carbonates (%)	Pyrite (%)	*TOC* (%)	G_{total} (m³/ton)
9#	2262.3–2283.8	55.0	42.1	2.6	0.2	1.1	1.0
8#	2283.8–2301.3	44.3	44.4	9.4	1.8	1.8	2.59
7#	2301.3–2313.3	39.9	48.3	10.7	1.1	1.7	2.29
6#	2313.3–2322.7	40.0	48.8	10.2	1.0	1.7	2.09
5#	2322.7–2332.8	36.7	52.1	9.3	2.0	2.4	3.53
4#	2332.8–2343	31.4	52.9	13.7	2.1	2.4	3.26
3#	2343–2356.3	20.7	66.5	9.8	3.1	3.5	5.0
2#	2356.3–2357.3	14.6	68.5	12.3	4.6	4.7	6.97
1#	2357.3–2372	19.7	69.7	8.1	2.4	3.6	5.67

Fig. 5 Conventional logs curves distribution of well JY-1X before **a** and after **b** standardization process
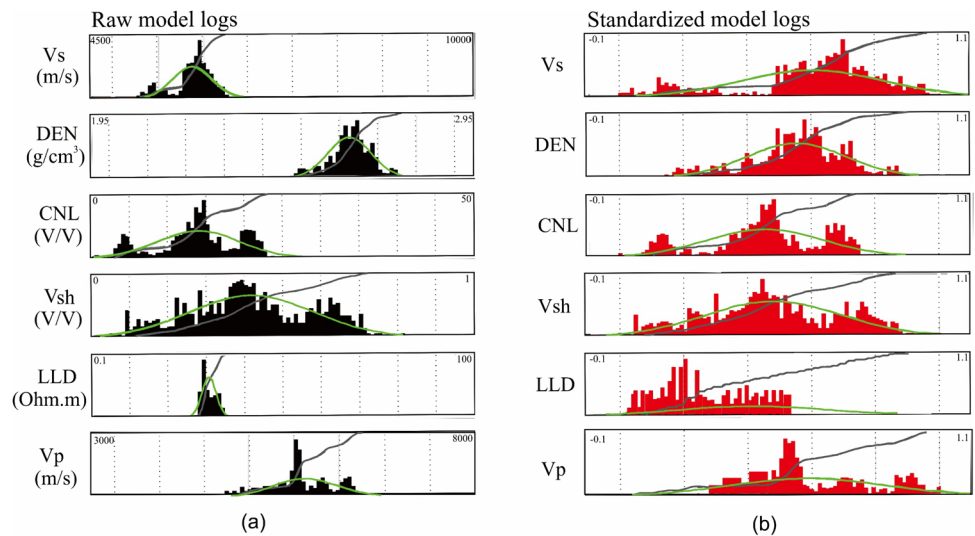
attributes and can be totally obtained using logging data. Additionally, it can be remarked that the integration of these parameters can reliably evaluate reservoir sequence and cluster behaviors. The method was computed using the face image module of Geolog 20.0, and the algorithm can be summarized essentially in five steps with different corresponding mathematical relationships.

(1) Using logging input data, the neighbor index (*NI*) is calculated, helping to estimate the connection between similarity measures (graph construction). The Euclidean distance between two samples *x* and *y* is defined by Eq. (17), while the *NI* calculation for a given measurement point *x* is presented below (Eq. 18):

$$\text{Dist}\,(x,y) = \sqrt{\sum_{i=1}^{N}(x_i - y_i)^2} \qquad (17)$$

$$s(x) = \sum_{n=1}^{N=1} \exp(-m/a) \qquad (18)$$

(2) Using a hierarchical clustering algorithm, the KNN attractions are generated based on the calculated *NI* values in the first step (graph partitioning):

$$S_{\max} = \underset{i=1,N}{\text{Max}}\left\{S(x_i)\right\} \qquad (19)$$

$$S_{\min} = \underset{i=1,N}{\text{Min}}\left\{S(x_i)\right\} \qquad (20)$$

$$\text{NI}(x) = \frac{S(x) - S_{\min}}{S_{\max} - S_{\min}} \qquad (21)$$

(3) Calculate the kernel representative index (*KRI*) necessary for generating a confident range in the determination of the number of clusters. The *KRI* integrates *NI*(*x*) with both a neighborhood function (*M*) and a distance function (*D*). The subgraphs are successively refined by recursively applying graph partitioning until the desired level of resolution is reached (clustering at multiple resolutions):

$$\text{KRI}(x) = \text{NI}(x) \times M \times D \qquad (22)$$

(4) Merging those initial small groups to form final clusters based on the nearest neighbors' attraction power. Clusters are identified based on the final partitioned subgraphs. Different clustering criteria, such as modularity or conductance, are used to define and evaluate the quality of the resulting clusters (cluster identification);

(5) Final distribution of the new data is accomplished, and clusters are analyzed by applying a multi-resolution approach to classify the reservoir. Geological characteristics and formation delimitations of the reservoir were considered during the MRGC process to minimize errors.

Results and discussion

Mineral comprehensive evaluation

Mineral composition results from ECS and NMR tests (Fig. 4) show that shale composition of the pilot well JY-1X is heterogeneous, with four different groups of minerals in different proportions (Fig. 4a). The principal identified minerals are siliceous minerals, essentially quartz and feldspar, with an average mass percentage relatively high; carbonate minerals (calcite, dolomite, and limestone); clay content (illite, chlorite, and kaolinite); and sulfide mineral (pyrite). This depth-based mineralogical composition sequence variation suggests substitutions in shale structure within the reservoir with new pore occupations during the burial process and therefore reflects the basin complexity (Omer et al. 2018). *TOC* content from cores has an average of 2.5%, and shale gas quality of layers 1#–5# can be considered relatively good, with *TOC* superior to 2%. G_{total} has a range of average values that are relatively low, between 1 and 6.97 m^3/ton, with highest values in the deep zones of the well. This observation was expected as old sediments under physico-chemical factors tend to generate more organic matter than relatively young layers (normal diagenesis process). Minerals, G_{total}, and their equivalent proportions are presented in Table 2. Figure 4b indicates that the clay in these samples

Table 3 Statistics of the main conventional logging parameters of well JY-1X

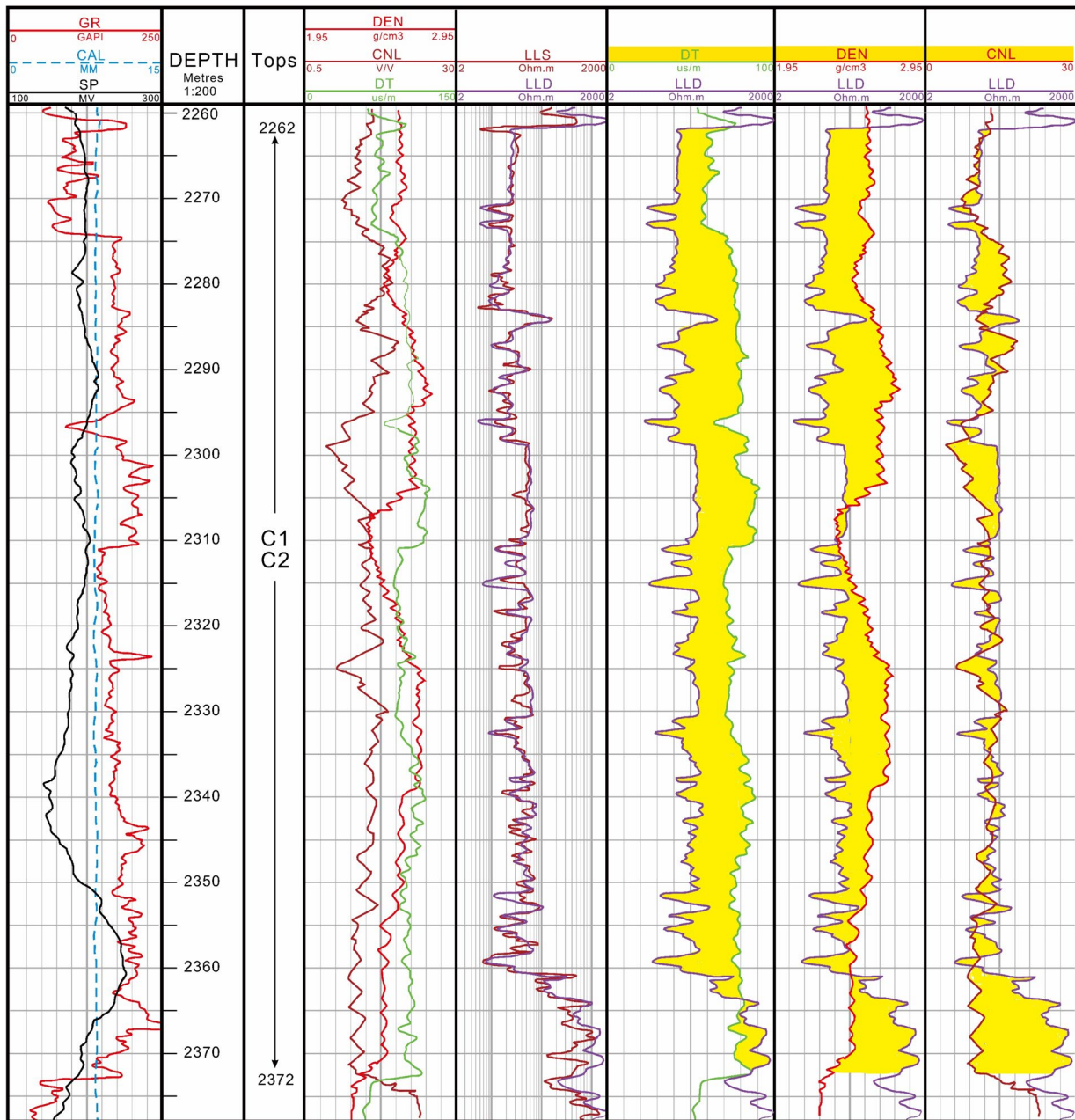|	GR (GAPI)	DEN (g/cm^3)	DT (µs/m)	CNL (V/V)	LLD (Ohm.m)	LLS (Ohm.m)
Minimum	31.99	2.41	51.65	0.63	5.40	5.32
P10	90.78	2.54	59.54	4.88	15.80	14.95
Mean	166.12	2.63	75.21	14.00	173.33	164.74
P90	208.42	2.71	84.43	20.97	573.58	537.22
Maximum	279.24	2.79	90.72	29.07	2829.73	2614.25

Fig. 6 Display of the main logging attributes of well JY-1X

mainly contains illite, with an average percentage of 65%. Chlorite and kaolinite average contents are 12.3 and 13.9%, respectively, while the mixtures of illite and smectite have a proportion of 8.8%.

Main reservoir properties

The modeling curves were selected from pilot well JY-1X, which include V_s, DEN, CNL, V_{sh}, LLD, and V_p, as presented

in Fig. 5. To eliminate the dimensional error between different modeling curves, the curves were standardized before modeling. The ANN method was used to fit the conventional logging curves of the pilot well, and the model was applied to other wells. ANN is a common neural network modeling technique for classification and recognition (Dixit et al. 2020). The method has three layers: input, hidden, and output, and it exhibits a multilayer feed-forward network trained via error backpropagation (Zhao et al. 2022).
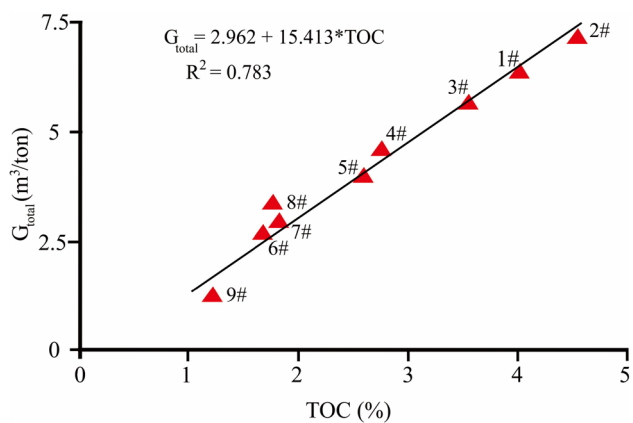
Fig. 7 Correlation between G_{total} and TOC

Therefore, Fig. 5a displays curves before standardization (original curve distributions), and Fig. 5b displays the results of the standardization process.

The statistical results of conventional logs are presented in Table 3 in terms of minimum, mean, percentiles (P10 and P90), and maximum. Logging responses show that the skeletal formation density is about 2.63 g/cm^3. Additionally, the measured density in well JY-1X is relatively smaller in the lower section of Longmaxi and upper section of Wufeng formations (2320–2360 m), which is a sign of rich organic shale presence. Higher LLD values were obtained in the deepest zones, with average values ranging from a few and several tens of ohm-meters to more than five hundred ohm-meters.

Figure 6 presents a summary of conventional logging curves for well JY-1X. From the left of the plot, parameters
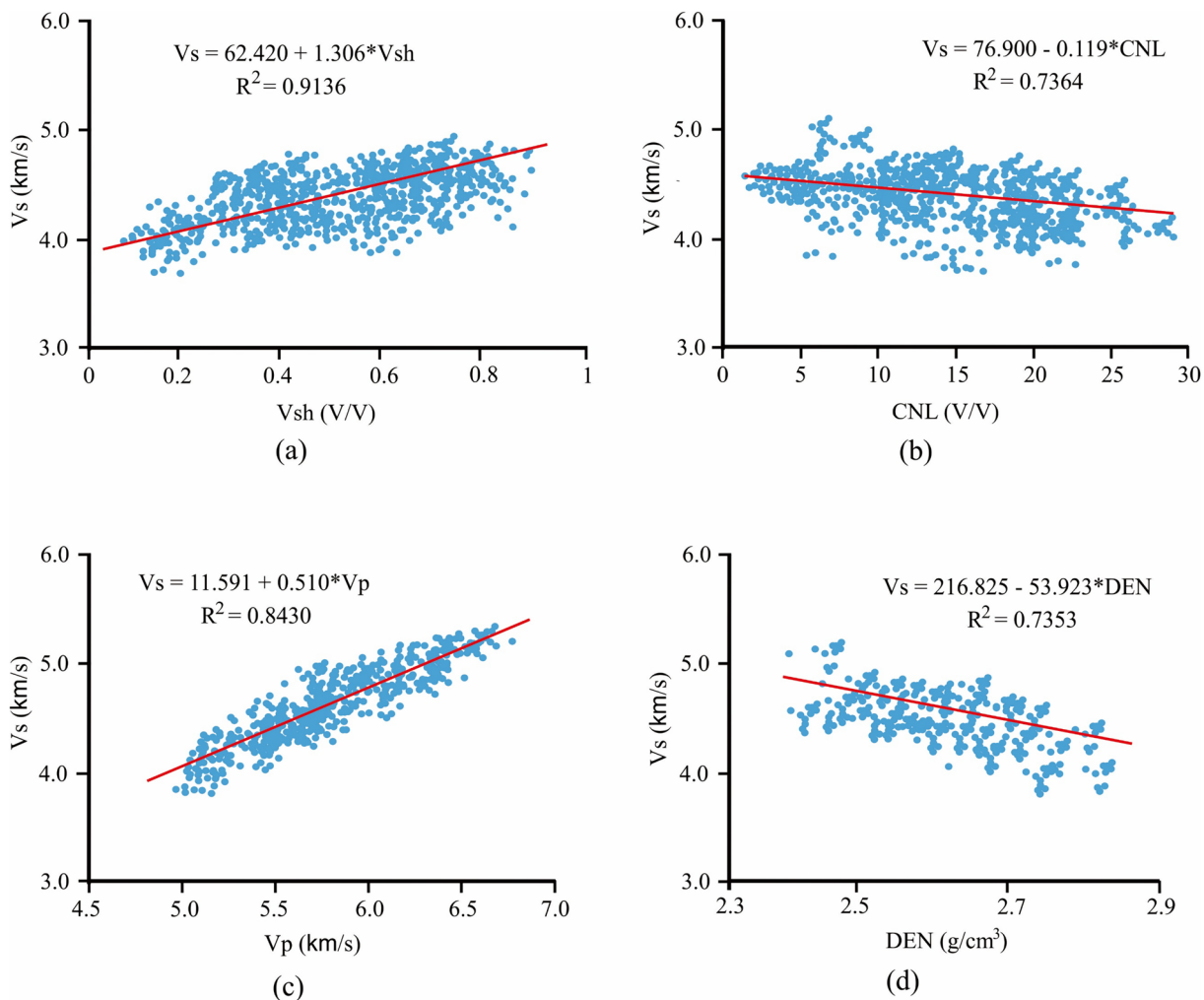
Fig. 8 Different cross-plots results. **a** V_s versus V_{sh}, **b** V_s versus CNL, **c** V_s versus V_p, and **d** V_s versus DEN of well JY-1X

Table 4 Average rock mechanical properties in well JY-1X

Layer umber	S_H (MPa)	S_h (MPa)	S_V (MPa)	Pp (MPa)	S_H–S_h (MPa)	S_V–Pp (MPa)	$(S_H$–$S_h)/(S_V - Pp)$	E (MPa)	μ (MPa)	Brittleness (%)	
										BI_1	BI_2
9#	50.17	48.62	55.52	32.33	1.55	23.19	0.06	28.16	0.29	50.25	42.12
8#	50.34	47.62	53.68	33.45	2.72	20.23	0.13	25.63	0.40	55.45	48.56
7#	48.11	42.23	49.25	33.95	5.88	15.3	0.38	33.23	0.36	65.50	53.69
6#	46.31	40.62	51.74	32.63	5.69	19.11	0.29	31.26	0.28	59.47	47.32
5#	47.33	43.46	50.17	30.35	3.87	19.82	0.19	25.4	0.19	60.25	52.33
4#	49.07	46.99	53.68	33.96	2.08	19.72	0.10	27.4	0.29	69.45	59.3
3#	50.25	45.02	51.09	32.04	5.23	19.05	0.23	30.5	0.32	69.50	58.96
2#	48.26	41.23	51.13	33.22	7.03	17.91	0.39	24.7	0.29	59.20	48.96
1#	48.63	46.02	52.32	32.05	2.61	20.27	0.12	32.6	0.29	70.50	56.99

in track 1 are SP, CAL, and GR logs. Tracks 4 and 5 present DT, CNL, DEN, LLD, and LLS. The relatively low mean GR values are associated with the deep and semideep shale sedimentary environment, which generates a low number of absorbed radioactive substances. CNL values indicate high values of neutrons in the reservoir due to the fine-grained reservoir composition. Moreover, due to the high bound water content, neutrons in the reservoir quickly attenuate, resulting in these high CNL curve responses. Track 6 illustrates the superposition of LLD and DT curves, which indicate the presence of clay minerals and organic matter. Track 7 shows the superposition of LLD and DEN curves, which suggests the presence of light minerals and low conductivity of organic matter. Track 8 displays the combination of LLD and CNL, confirming the organic matter richness of the reservoir. Therefore, this approach based on logging curves characteristic responses can be extended to other wells to qualitatively identify the reservoir.

Figure 7 presents the intersection of G_{total} and *TOC*. The positive correlation between the two parameters is high ($R^2 = 0.783$) and suggests that organic matter plays a significant role in controlling the reservoir gas content. The regression shows that G_{total} increases by an average of 2.962 m^3/ton for each additional increase in *TOC* percentage. Furthermore, it shows that older layers are rich in organic matter and generate more gas than younger layers, which reveals a normal sediments depositional environment in this section. Figure 8 compares the correlations between V_{sh}, DEN, CNL, and V_p versus V_s and identifies two trends. The negative linear correlation of V_s versus CNL and DEN indicates a change in shale structure (substitutions) and the apparition of new minerals such as mica, siderite, anatase, and different crystallites into the pores (Sakhaee-Pour and Bryant 2015; Gou et al. 2019). On the other hand, the positive correlation

of V_s versus V_{sh} and V_p indicates a proportional shale distribution horizontally and vertically in the reservoir.

The main geomechanical properties results, which include the brittleness index and anisotropy component of well JY-1X, are presented in Table 4 and Fig. 9. *BI* values for both methods mainly increase with depth and exhibit brittle shales. Only BI_2 of formation layers 6# and 9# can be considered less brittle. The other seven layers are brittle, with average values varying between 48 and 70.50%. BI_1 values are higher than BI_2, with variations of ±10% in the zones. Thus, gas in the high brittle layers of the reservoir can be considered highly compressible and susceptible to hydraulic fracturing. The increase in S_H, S_h, and S_v is non-uniform with depth, and the relationship is nonlinear due to reservoir heterogeneity and complexity. However, $S_v > S_H > S_h$ suggests a normal stress regime with fault systems essentially oriented NWW (main deformation direction) at each reservoir depth. *Pp* ranged between 30.35 and 33.96 MPa, averaging 32.66 MPa. The earth pressure coefficient, defined as the ratio of horizontal and vertical effective stresses in the reservoir, is relatively high for most zones. Values range from 0.10 to 0.39, except zone 2#. These values reflect the natural stability of this well reservoir and can be used as a basis for evaluating the other wells during the reservoir development phase. Figure 9 summarizes the logging curves of geomechanical parameters. Track 4 contains V_p and V_s. Fracture pressure gradients, E and μ, are presented in track 5. Track 6 displays P_p from Eaton–Yale method and rupture pressure curves. S_h, S_H, S_V, and the horizontal stress difference are illustrated in track 7, while BI_2 is presented in track 8.

Electro-facies analysis

Facies classification and modeling were performed on the set of wells based on GR, *TOC*, BI_2, S_v, S_H, and S_h.
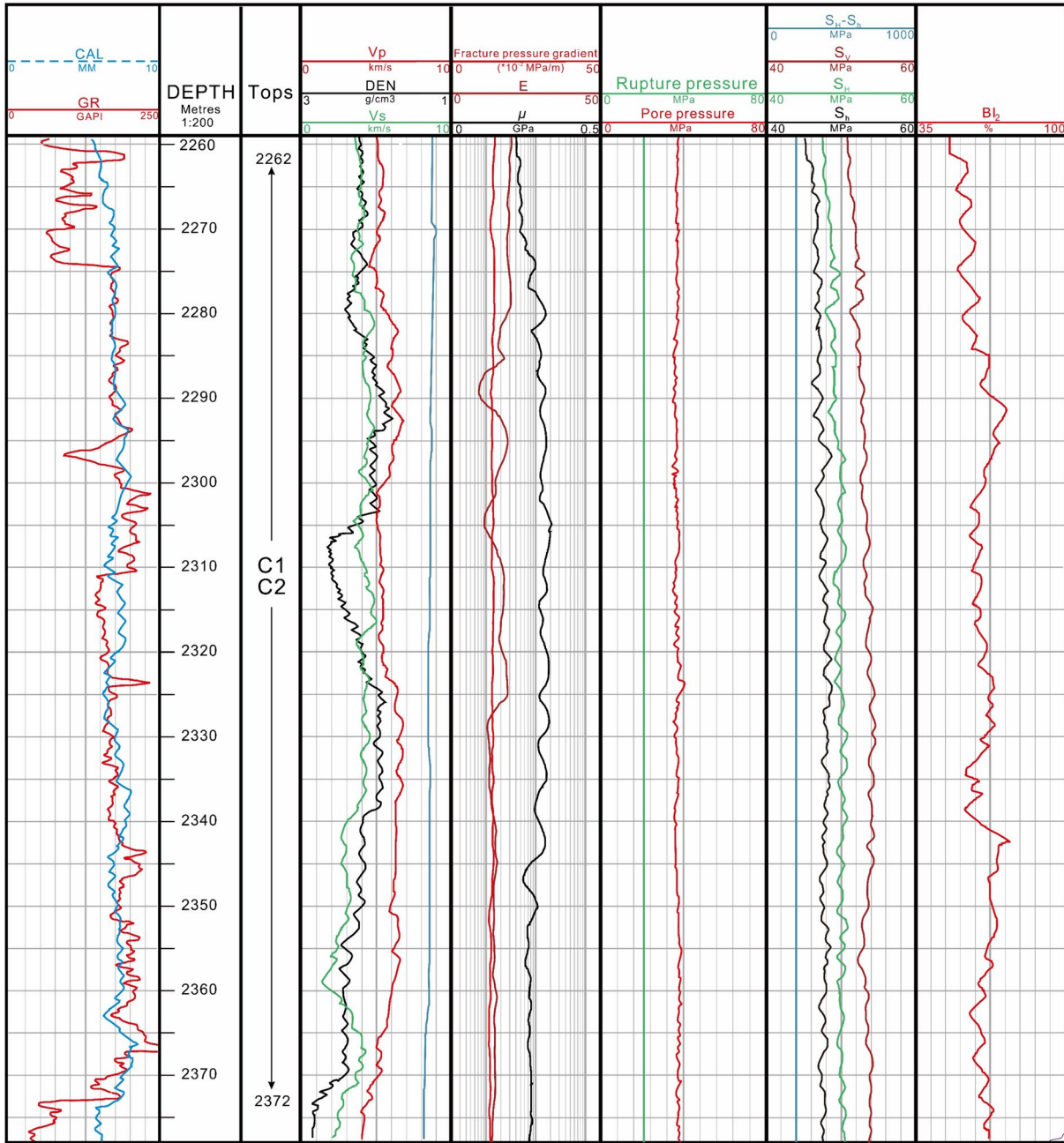
Fig. 9 Results of rock geomechanical properties for well JY-1X

Figure 10 illustrates the distribution characteristics of these parameters before and after the standardization process. It can be observed that the raw values of these six curves were dimensionally dispersed, especially for the computed stress curves. Standardization eliminated these curve errors caused by the dimensional differences while removing eventual outliers within the logs. After the merging process and based on the final cluster weights,

five main EFs were identified with the clustering sequence of the six parameters. The corresponding histograms from the normalized self-organizing map (SOM) of each parameter (Fig. 11) indicate a homogeneous shale sequence with the five EFs and a relatively good clustering effect. From the cross-plots and reports in Fig. 11, it can be observed that EF2 and EF3 provide the best reservoir quality with characteristics similar to the lower Longmaxi formation

Fig. 10 Logs data distribution before **a** and after **b** the standardization process
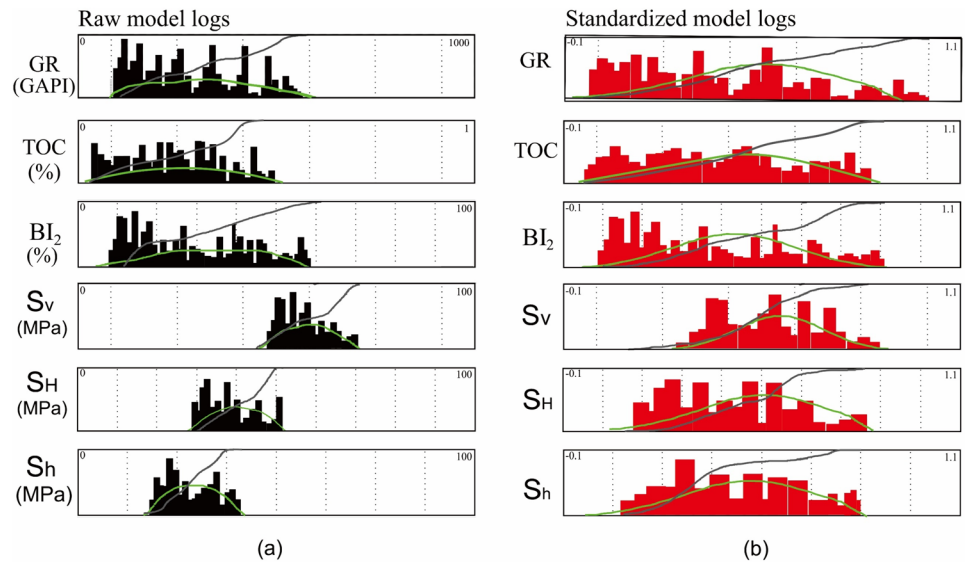
(see Tables 1, 2 and 3). On the other hand, EF4 and EF5 show characteristics that suggest a medium reservoir quality, with similar features associated with the upper Longmaxi formation. The worst reservoir can be associated with EF1 in the deepest depths of the well (Wufeng formation).

Figure 12 displays the distribution of the obtained EFs within the well JY-1X. GR and *TOC* are presented in track 2, while S_v and BI_2 are displayed in tracks 3 and 4. Track 5 contains S_H and S_h, whereas EFs by MRGC and reservoir classification results are indicated in track 6. Figure 13 shows box diagrams that give the final description of the EFs distributions of the set of wells. This interpretation is based on the integration of their different characteristics correlated with the pilot well JY-1X. Therefore, EF2 and EF3, identified in the lower Longmaxi unit, are characterized by medium GR response values and relatively high mean values of *TOC* coupled with high quantities of brittle (Table 5). Furthermore, the mean values of S_V, S_H, and S_h vary between 43.89 and 53.96 MPa, suggesting favorable reservoir sections. The medium-quality reservoir in the upper Longmaxi section with EF4 and EF5 is characterized by medium brittle minerals with GR values of 185.98 and 193.44 GAPI, respectively. S_V and S_H mean values vary between 38.63 and 45.04 MPa, while *TOC* is 2.92% and 2.10%, respectively, for EF3 and EF4. EF1 has the worst reservoir quality due to its high GR responses, which reach more than 200 GAPI, low *TOC* (less than 1.50%), and less brittle minerals (about 44.56%). Table 5 summarizes these statistical results of the clustering and EFs parameters corresponding values in terms of mean values.

Implications for reservoir development

The main purpose of reservoir characterization is to provide a basis for hydraulic fracturing operations and reservoir simulation models (Omer et al. 2018). Additionally, identifying brittle zones is essential in fracture design to evaluate fracture barriers that control vertical development. Therefore, accurate *BI* is crucial in these processes, knowing that this parameter is subject to uncertainties. *BI* was evaluated in well JY-1X using two methods (BI_1 and BI_2), and Fig. 14 presents their intersection results. Though the correlation coefficient is relatively high ($R^2 = 0.723$), two trends can be identified in this reservoir section. A trend with a perfect correlation between the two estimated *BI* methods (layers 4#, 6#, and 9#). Homogenous mineralogy and physicochemical parameter variations could explain this, as sediment remains compact in these zones (Liu et al. 2020). The second trend, where the two types of *BI* are not perfectly correlated, is dominant and includes reservoir layers 1#, 2#, 3#, 5#, 7#, and 8#. This difference can be explained by variations in *BI* evaluation based on mineral composition because this approach only depends on rock mineral composition and does not consider the interaction between internal factors in the reservoir, such as mineral replacement, dissolution or overgrowth, and the impact of confining pressure mechanisms (Mews et al. 2019; Meng et al. 2020). Furthermore, *BI* determination approach based on elastic parameters major limitation is that many of the formulas and techniques used are only applicable and effective in certain cases, which limits their applicability and efficiency (Qian et al. 2020). Therefore, as this study reduced the difference between the
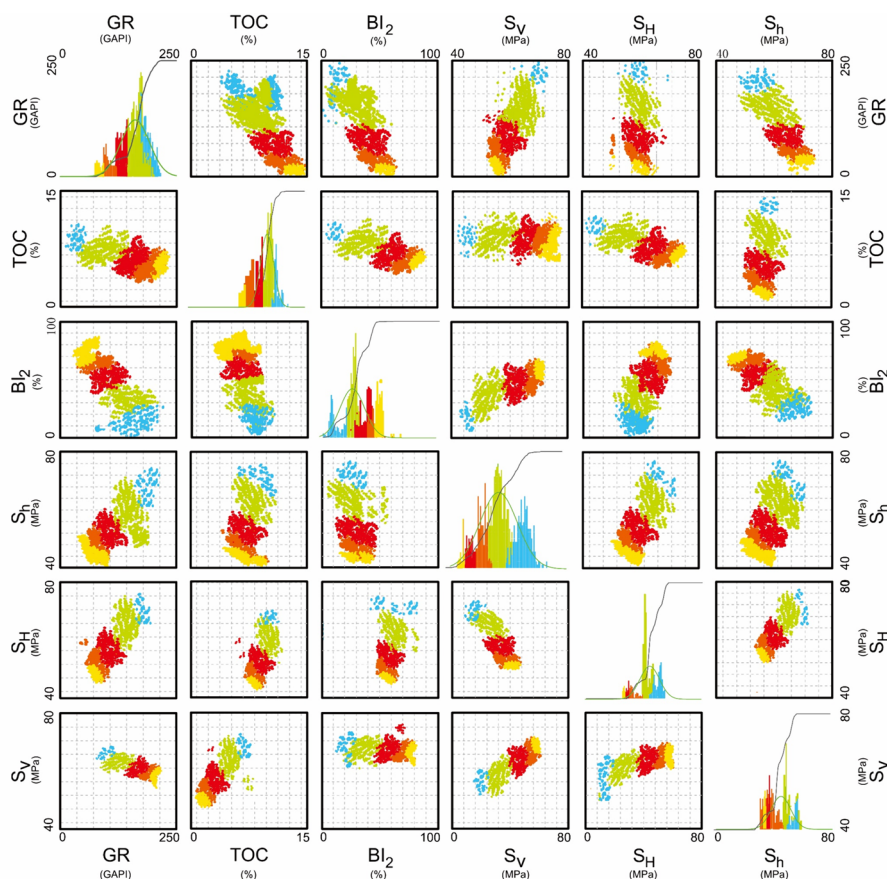
NAME	COL	WEIGHT	GR	TOC	BI$_2$	S$_V$	S$_H$	S$_h$
FACIES_1		137						
FACIES_2		936						
FACIES_3		798						
FACIES_4		298						
FACIES_5		359						

Fig. 11 SOM classification and derived EF histograms based on standardized data from GR, *TOC*, *BI*$_2$, *S*$_v$, *S*$_H$, and *S*$_h$

two *BI* methods by including external petrophysics parameters, it suggested using the appropriate method based on the case.

As related in the literature (Hu et al. 2018; Gou et al. 2021; Xiong et al. 2022), development studies on the Jiaoshiba area are still in the early exploration stages with unsolved problems. Therefore, the proposed workflow can be used to identify barriers and potential favorable layers for fractures. Hydraulic cracks are extended perpendicular to the least principal stress, particularly in deep formations, due to significant overburden stress in the reservoir. Thus, *S*$_h$ is the least principal stress and can be considered, in this case, to be critical for pre-fracture stimulation (Zoback et al. 2003; Alessa et al. 2022). However, this approach is limited because *S*$_h$ can mainly be extended laterally, causing difficulty in developing a system for gas recovery (Hakiki and Shidqi 2018; Esatyana et al. 2021). This study categorized shale into brittle and less brittle types with relatively favorable petrophysical characteristics. Therefore, parameters such as rock brittleness and shale porosity integrated into the model ensure its efficiency and reliability. Figure 15 illustrates
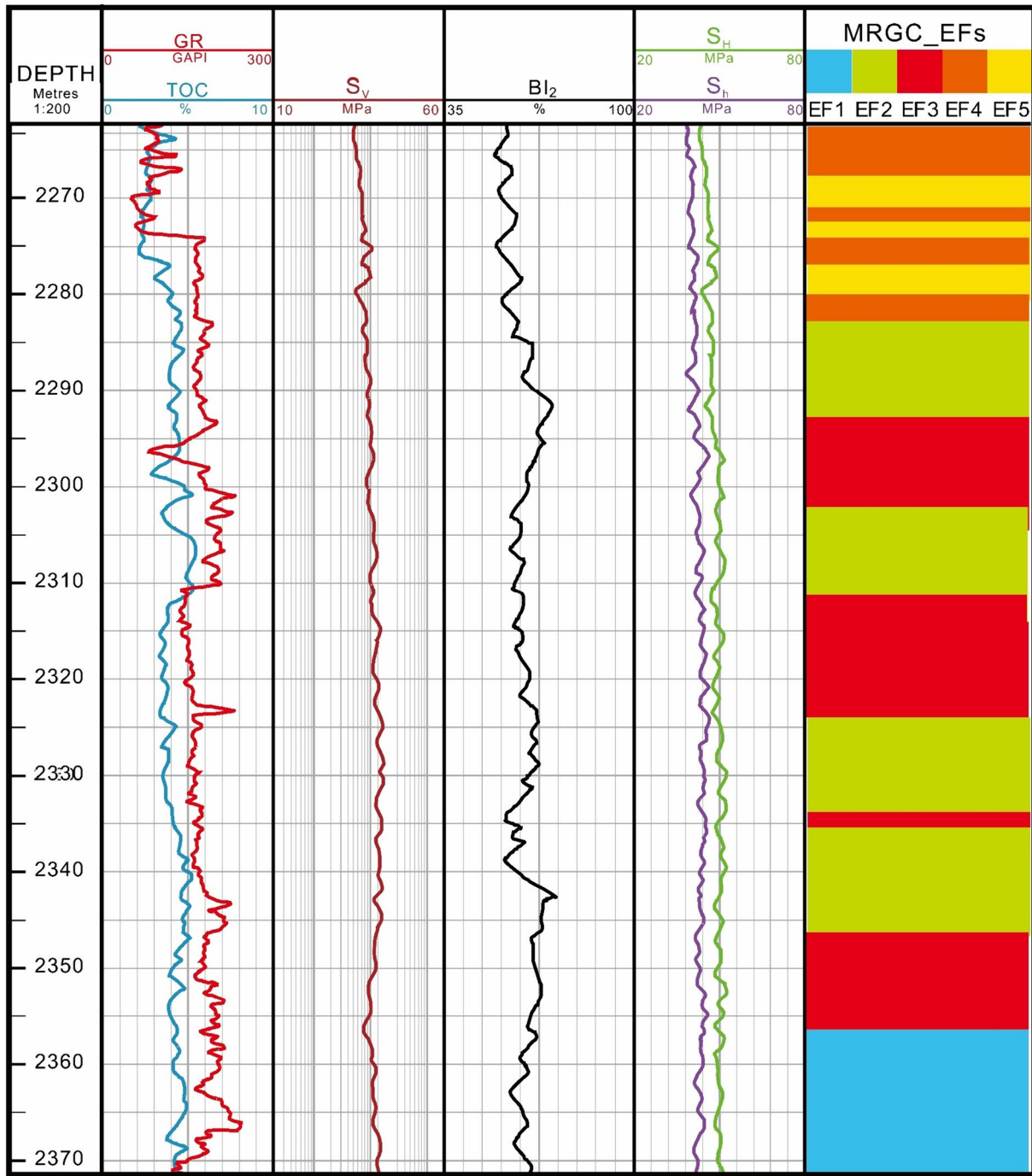
Fig. 12 EFs classification of shale sequence in well JY-1X

a correlation between brittleness index, mineralogy, and other petrophysical and geomechanical characteristics. A strong lateral correlation is observed between S_h, EFs, *BI*, and potential fracture zones. There are many blue-colored layers, considered favorable for fracturing because their organic richness and total porosity are also relatively high, while there are certain visible fracture barriers that are black in color, possibly representing fracture attenuators.
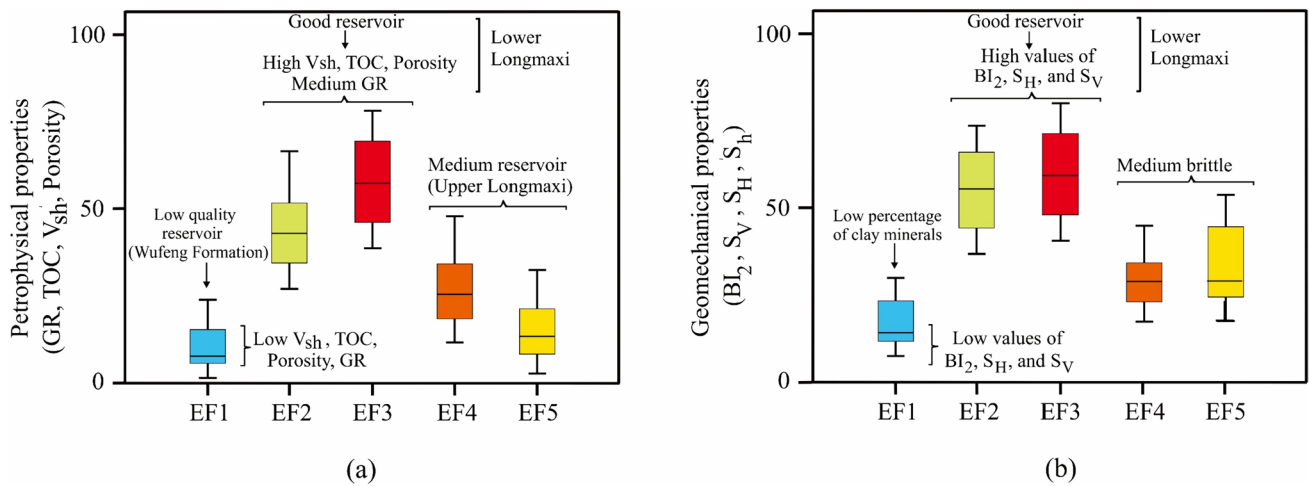
Fig. 13 Boxplot showing the summary characteristics of the reservoir

Table 5 Reservoir EFs statistics from MRGC

Facies	Weight	GR (GAPI)	TOC (%)	BI_2 (%)	S_h (MPa)	S_H (MPa)	S_v (MPa)
EF1	137	207.25	1.26	44.56	29.20	31.29	32.59
EF2	936	162.12	3.63	66.52	46.89	50.29	51.32
EF3	798	150.80	4.56	69.96	43.89	51.89	53.96
EF4	298	185.98	2.92	62.36	38.63	39.08	40.98
EF5	359	193.44	2.10	50.36	41.36	43.78	45.04
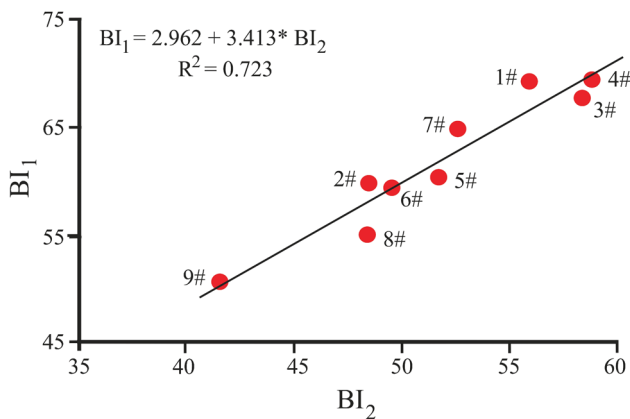
Fig. 14 Cross-plot of measured and calculated BI

This approach, which combines these parameters, could be further developed and completed with reservoir simulation tests during the reservoir development phase. Formation porosity and shale porosity are, respectively, presented in tracks 3 and 4. Tracks 11 and 12 contain mineral composition, favorable fracture zones, and barriers. Fracture characteristics were computed and extracted from the integration of stress parameters, mineral brittleness, and petrophysical properties.

Conclusions

In this study, an approach that combines the main petrophysical and geomechanical properties was developed for shale gas reservoir evaluation and electro-facies (EF) classification. Parameters, including shale volume (V_{sh}), total organic carbon (TOC), brittleness index (BI), and stress components (S_v, S_H, and S_h), were estimated using wireline logs in a series of wells. Reservoir classification was investigated through cluster analysis using the nonparametric unsupervised multi-resolution graph-based clustering (MRGC) method, which uses the artificial neural network (ANN). The approach combines K-nearest neighbors (KNN) and graphical algorithms for reservoir evaluation. The unsupervised method provided clusters with mathematical limits while removing the subjectivity associated with manual interpretations. Output clusters were differentiated according to their intrinsic properties, which are associated with the reservoir characteristics. Based on the results, the following conclusions were reached:

- Petrophysical and geomechanical characteristics of the pilot well JY-1X were extracted to provide a basis for the correlation and integration of the series of wells. Necessary corrections were made to the raw logging data
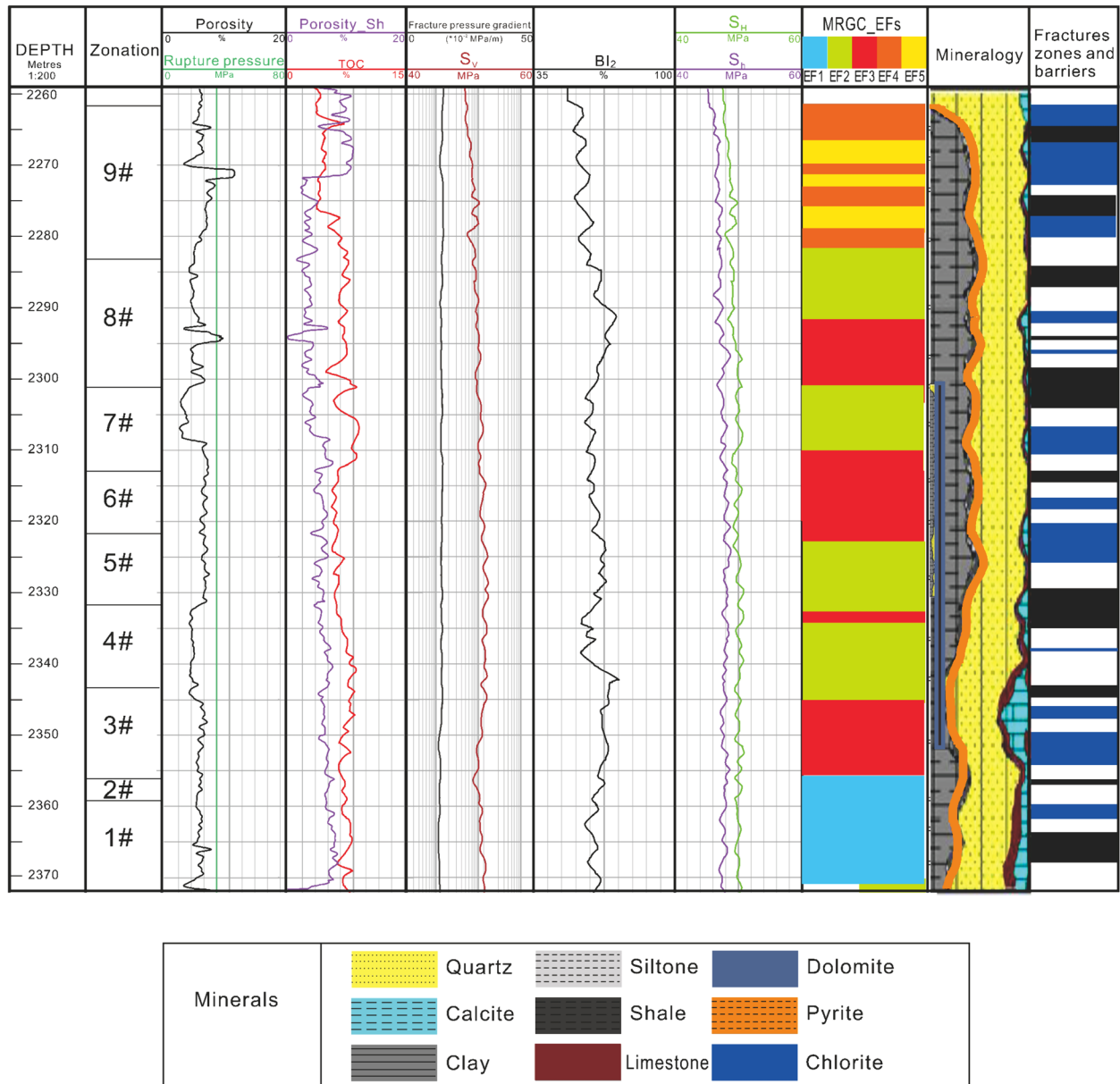
Fig. 15 Integrated model for identifying potential favorable zones and fracture barriers in well JY-1X

for the set of wells to eliminate curve errors caused by dimensional differences and remove outliers for each log.

- *TOC* values of the reservoir range between 1.1 and 4.7%, with an average value of 2.54%. S_v, S_H, and S_h evaluations indicate a normal stress regime with hydraulic fracture systems that are perpendicular to the minimum horizontal stress component at each measured depth of the reservoir ($S_v > S_H > S_h$). The Eaton–Yale method, correcting overpressure and considering basin history, was used to determine pore pressure, with values ranging from 30.35 to 33.96 MPa.

- *BI* results were classified as brittle (conducive to fractures) and less brittle, depending on the layer. Carbonates and quartz are considered brittle minerals in this reservoir, while clay minerals are the most ductile minerals.

- The clustering process by MRGC after the merging process and the final cluster weight properties identified 5 EFs, with results correlated to the pilot well interpretations. EF2 and EF3 displayed the best reservoir quality with medium gamma-ray (GR) values, high *TOC* coupled with high *BI* and CNL. EF4 and EF5 were characterized as medium reservoir quality with relatively high GR and medium CNL readings. EF1 showed the worst reservoir quality due to its high GR (about 207.25 GAPI), low *TOC* (less than 1.50%), and less *BI* (about 44.56%).

- The research findings represent significant time-saving and low-cost analysis in the interpretation of a large set of data. The combined results of rock *BI* characteristics with S_V, S_H, S_h and petrophysical properties can be used as the basis for reservoir simulation and hydraulic fracturing processes. Further studies can extend the developed approach by including additional reservoir characteristics such as capillary pressure and relative permeability.

Data availability All data generated or analyzed during this work are available from the corresponding author on reasonable request.

Declarations

Conflict of interest The authors declare that they have no known competing financial interests or personal relationships that could have appeared to influence the work reported in this paper. There are no conflicts of interest to declare.

References

Al Hasan R, Saberi MH, Riahi MA, Manshad AK (2023) Electro-facies classification based on core and well-log data. J Pet Explor Prod Technol 13:2197–2215. https://doi.org/10.1007/s13202-023-01668-5

Alessa S, Sakhaee-Pour A, Sadooni FN, Al-Kuwari HA (2022) Capillary pressure correction of cuttings. J Petrol Sci Eng 217:110908. https://doi.org/10.1016/j.petrol.2022.110908

Alipour M, Sakhaee-Pour A (2023) Application of Young-Laplace with size-dependent contact angle and interfacial tension in shale. Geo Sci Eng 231:212447. https://doi.org/10.1016/j.geoen.2023.212447

Alipour M, Esatyana E, Sakhaee-Pour A, Sadooni FN, Al-Kuwari HA (2021) Characterizing fracture toughness using machine learning. J Pet Eng 200:108202. https://doi.org/10.1016/j.petrol.2020.108202

Alipour M, Kasha A, Sakhaee-Pour A, Sadooni FN, Al-Kuwari HA (2022) Empirical relation for capillary pressure in shale. J Pet Eng 63(05):591–603. https://doi.org/10.30632/PJV63N5-2022a2

Bowers GL (1995) Pore pressure estimation from velocity data: accounting for overpressure mechanisms besides undercompaction. SPE Drilling Complet 10:89–95. https://doi.org/10.2118/27488-PA

Chen F, Lu S, Ding X, He X (2018) Shale gas reservoir characterization: a typical case in the Southeast Chongqing of Sichuan Basin. China Plos One 13(6):e0199283. https://doi.org/10.1371/journal.pone.0199283

Clavier C, Hoyle W, Meunier D (1971) Quantitative interpretation of thermal neutron decay time logs: part I. fundamentals and techniques. J Pet Technol 23(06):743–755. https://doi.org/10.2118/2658-A-PA

Dixit N, McColgan P, Kusler K (2020) Machine learning-based probabilistic lithofacies prediction from conventional well Logs: a case from the Umiat Oil Field of Alaska. Energies 13(18):4862. https://doi.org/10.3390/en13184862

Dong D, Shi Z, Guan Q, Jiang S, Zhang M, Zhang C, Wang S, Sun S, Yu R, Liu D, Peng P (2018) Progress, challenges and prospects of shale gas exploration in the Wufeng-Longmaxi reservoirs in the Sichuan Basin. Nat Gas Ind B 5(5):415–424. https://doi.org/10.1016/j.ngib.2018.04.011

Dos Passos FV, Braga MA, Carelli TG, Plantz JB (2020) Electro-facies classification of ponta grossa formation by multi-resolution graph-based clustering (MRGC) and self-organizing maps (SOM) methods. Braz J Geophys 38(1):52–61. https://doi.org/10.22564/rbgf.v38i1.2

Eaton BA (1975) The equation for geopressure prediction from well logs. In: Fall Meeting of the Society of Petroleum Engineers of AIME, Dallas https://doi.org/10.2118/5544-MS

Esatyana E, Sakhaee-Pour A, Sadooni FN, Al-Kuwari HA (2020) Characterizing Nanoindentation of shale cuttings and its application to core measurements. Petrophysics 61(05):404–416. https://doi.org/10.30632/PJV61N5-2020a1

Esatyana E, Alipour M, Sakhaee-Pour A (2021) Characterizing anisotropic fracture toughness of shale using nanoindentation. SPE Reserv Eval Eng 24(03):590–602. https://doi.org/10.2118/205488-PA

Gou Q, Xu S (2019) Quantitative evaluation of free gas and adsorbed gas content of Wufeng-Longmaxi shales in the Jiaoshiba area, Sichuan Basin, China. Adv Geo-Energy Res 3(3):258–267. https://doi.org/10.26804/ager.2019.03.04

Gou Q, Xu S, Hao F, Shu Z, Zhang Z (2021) Making sense of microfractures to the Longmaxi shale reservoir quality in the Jiaoshiba area, Sichuan Basin, China: implications for the accumulation of shale gas. J Nat Gas Sci Eng 94:104107. https://doi.org/10.1016/j.jngse.2021.104107

Hakiki F, Shidqi M (2018) Revisiting fracture gradient: comments on a new approaching method to estimate fracture gradient by correcting Matthew-Kelly and Eaton's stress ratio. J Pet 4:1–6. https://doi.org/10.1016/j.petlm.2017.07.001

Hu F, Huang W, Li J (2018) Effects of structural characteristics on the productivity of shale gas wells: a case study on the Jiaoshiba Block in the Fuling shale gas field, Sichuan Basin. Nat Gas Ind B 5:139–147. https://doi.org/10.1016/j.ngib.2018.02.001

Jia Y, Tang J, Lu Y, Lu Z (2021) Laboratory geomechanical and petrophysical characterization of Longmaxi shale properties in Lower Silurian Formation. China Mar Pet Geol 124:104800. https://doi.org/10.1016/j.marpetgeo.2020.104800

Liu B, Zhao X, Fu X, Yuan B, Bai L, Zhang Y, Ostadhassan M (2020) Petrophysical characteristics and log identification of lacustrine shale lithofacies: A case study of the first member of Qingshankou Formation in the Songliao Basin, Northeast China. J Interpret Res 8(3):SL45–SL57. https://doi.org/10.1190/INT-2019-0254.1

Liu B, Tan C, Huai Y, Zhang H, Feng Z (2023) Multiparameter logging evaluation of Chang 7_3 Shale Oil in the Jiyuan Area, Ordos Basin. Geofluids. https://doi.org/10.1155/2023/1672207

Meng F, Wong LNY, Zhou H (2020) Rock brittleness indices and their applications to different fields of rock engineering: a review. JRMGE 13(1):221–247. https://doi.org/10.1016/j.jrmge.2020.06.008

Mews KS, Alhubail MM, Barati RG (2019) A review of brittleness index correlations for unconventional tight and ultra-tight reservoirs. Geosci 9(7):319. https://doi.org/10.3390/geosciences9070319

Mkinga OJ, Skogen E, Kleppe J (2020) Petrophysical interpretation in shaly sand formation of a gas field in Tanzania. J Pet Explor Prod Technol 10:1201–1213. https://doi.org/10.1007/s13202-019-00819-x

Nie H, Chen Q, Zhang G, Sun C, Wang P, Lu Z (2021) An overview of the characteristic of typical Wufeng-Longmaxi shale gas fields in the Sichuan Basin. China Nat Gas Ind B 8(3):217–230. https://doi.org/10.1016/j.ngib.2021.04.001

Omer I, Maqsood A, Askury AK (2018) Effective evaluation of shale gas reservoirs by means of an integrated approach to petrophysics and geomechanics for the optimization of hydraulic fracturing: a case study of the Permian Roseneath and Murteree Shale Gas reservoirs, Cooper Basin, Australia. J Nat Gas Sci Eng 58:34–58. https://doi.org/10.1016/j.jngse.2018.07.017

Ou C, Li C, Rui Z, Ma Q (2018) Lithofacies distribution and gas-controlling characteristics of the Wufeng-Longmaxi black shales in the southeastern region of the Sichuan Basin, China. J Pet Sci Eng 165:269–283. https://doi.org/10.1016/j.petrol.2018.02.024

Passey QR, Creaney S, Kulla JB (1990) A practical model for organic richness from porosity and resistivity logs. AAPG Bull 74(12):1777–1794

Perez R, Kurt M (2013) Brittleness estimation from seismic measurements in unconventional reservoirs: application to the Barnett Shale. SEG Int Exposition Annual Meet. https://doi.org/10.1190/segam2013-0006.1

Qian KR, Liu JZ, Zhou H, Liu XW, He ZL, Jiang DG (2020) Construction of a novel brittleness index equation and analysis of anisotropic brittleness characteristics for unconventional shale formations. Pet Sci 17:70–85. https://doi.org/10.1007/s12182-019-00372-6

Sakhaee-Pour A, Bryant SL (2012) Gas permeability of shale. SPE Res Eval Eng 15(04):401–409. https://doi.org/10.2118/146944-PA

Sakhaee-Pour A, Bryant SL (2015) Pore structure of shale. Fuel 1(143):467–475. https://doi.org/10.1016/j.fuel.2014.11.053

Sakhaee-Pour A, Li W (2016) Fractal dimensions of shale. J Nat Gas Eng 30:578–582. https://doi.org/10.1016/j.jngse.2016.02.044

Shen W, Luo Z, Ma T, Chen C, Qin C, Yang L, Xie K (2023) Quantitative studies on the characterization and evaluation of adsorbed gas and free gas in deep shale reservoirs. Energ Fuel 37(5):3752–3759. https://doi.org/10.1021/acs.energyfuels.2c04261`

Song Y, Zeng L, Gong F, Huang P, Lyu W, Dong S (2023) Petrophysical characteristics and identification parameters of the Jurassic continental shale oil reservoirs in the Central Sichuan Basin. J Geophys Eng 20(1):78–90. https://doi.org/10.1093/jge/gxac097

Terzaghi K, Peck RB, Mesri G (1996) Soil mechanics in engineering practice. John Wiley & Sons, UK

Xia Y, Zhou H, Zhang C, He S, Gao Y, Wang P (2022) The evaluation of rock brittleness and its application: a review study. Eur J Environ Civ Eng 26(1):239–279. https://doi.org/10.1080/19648189.2019.1655485

Xiong J, Li Y, Zhou S, Liu X, Han H, Liang L, Zhao J (2022) Reservoir Insights into the pore structure characteristics of the Lower Silurian Longmaxi Formation shale in the Jiaoshiba area, Southern Sichuan Basin, China. J Pet Explor Prod Technol 12:2857–2868. https://doi.org/10.1007/s13202-022-01486-1

Yale DP, Perez A, Raney R (2018) Novel pore pressure prediction technique for unconventional reservoirs. In: Unconventional Resources Technology Conference Houston. https://doi.org/10.15530/URTEC-2018-2901731

Yu C, Tran H, Sakhaee-Pour A (2018) Pore size of shale based on acyclic pore model. Transp Porous Media 124(2):345–368. https://doi.org/10.1007/s11242-018-1068-4

Zhao P, Ma H, Rasouli V, Liu W, Cai J, Huang Z (2017) An improved model for estimating the TOC in shale formations. Mar Pet Geol 83:174–183. https://doi.org/10.1016/j.marpetgeo.2017.03.018

Zhao C, Jiang Y, Wang L (2022) Data-driven diagenetic facies classification and well-logging identification based on machine learning methods: a case study on Xujiahe tight sandstone in Sichuan Basin. J Petrol Sci Eng 217(4):110798. https://doi.org/10.1016/j.petrol.2022.110798

Zheng Y, Liao Y, Wang Y, Xiong Y, Peng PA (2018) Organic geochemical characteristics, mineralogy, petrophysical properties, and shale gas prospects of the Wufeng-Longmaxi shales in Sanquan Town of the Nanchuan District. Chongqing AAPG Bull 102(11):2239–2265. https://doi.org/10.1306/04241817065

Zhu L, Chong Z, Zhang C, Wei Y, Zhou X, Cheng Y, Huang Y, Zhang L (2018) Prediction of total organic carbon content in shale reservoir based on a new integrated hybrid neural network and conventional well logging curves. J Geophys Eng 15:1050–1061. https://doi.org/10.1088/1742-2140/aaa7af

Zoback MD, Barton M, Brudy DA, Castillo DA, Finkbeiner T, Grollimund BR, Moos DB, Peska P, Ward CD, Wiprut DJ (2003) Determination of stress orientation and magnitude in deep wells. Int J Rock Mech Min 40:1049–1076. https://doi.org/10.1016/j.ijrmms.2003.07.001